SCIENCE CHINA
Information Sciences

• MOOP •

June 2024, Vol. 67, Iss. 6, 164201:1–164201:3
https://doi.org/10.1007/s11432-023-4027-x

Vector field path following for a micro flapping-wing robot

Haifeng HUANG[1,2,3], Yingte LIU[1,2,3], Tao NIU[1,2,3], Chang WANG[1,2,3], Yao ZOU[1,2,3] & Wei HE[1,2,3*]

[1]*School of Intelligence Science and Technology, University of Science and Technology Beijing, Beijing* 100083*, China;*
[2]*Institute of Artificial Intelligence, University of Science and Technology Beijing, Beijing* 100083*, China;*
[3]*Key Laboratory of Intelligent Bionic Unmanned Systems, Ministry of Education, University of Science and Technology Beijing, Beijing* 100083*, China*

Received 4 November 2023/Revised 9 January 2024/Accepted 27 February 2024/Published online 20 May 2024

Flapping-wing robots mimic the flight patterns of natural flying creatures, granting them natural camouflage. They hold promising applications in the military reconnaissance, urban surveillance, and various other fields [1–3]. However, the current limitations in size often restrict the suitability of existing bird-like flapping-wing robots, such as E-Flap [4] and USTBird [5], for indoor tasks. Furthermore, while micro flapping-wing robots such as Delfly and H2Bird excel in navigating confined spaces, their progress towards attaining stable autonomous flight capabilities requires further development [5]. Accurately following preplanned paths is essential for enabling micro flapping-wing robots to autonomously execute tasks. Among the path following algorithms currently in use, the vector field algorithm stands out for its ability to minimize cross-track error and control effort in guiding miniature air vehicles [6], but its application to micro flapping-wing robots has yet to be explored. This work presents two primary contributions. First, a novel X-wing flapping-wing robot capable of hovering and stable flight was designed. Second, a vector field-based guidance algorithm was proposed for the autonomous straight-line path following of the robot, and flight experiments verified the effectiveness of the control system.

Design of the experimental platform. The micro X-wing flapping-wing robot we designed, depicted in Figure 1(a), boasts a wingspan of 27 cm and a weight of 18 g. A micro motor, connected to a gear set, drives the wings to flap periodically. For turning control, the robot employs a micro servo to manipulate the T-shaped tail. Additionally, a communication module interfaces with the flight control board, enabling real-time connectivity with the upper computer. The robot's head and tail are equipped with five reflective markers, aiding recognition by the motion capture system, as depicted in Figure 1(b). This system swiftly captures position and quaternion data from the robot in motion, achieving a delay of less than two milliseconds. Subsequently, this data is transmitted to the upper computer for additional processing as shown in Figure 1(c).

Vector field based path following. Vector field guidance is a widely adopted technique that minimizes cross-track error while demanding minimal control efforts compared to other algorithms. The core aim of vector field path following is to establish a desired heading field and subsequently guide the robot to follow this field, enabling it to traverse along the predetermined path [7]. As vector field guidance operates on geometric principles, the control law's calculation depends on the target path chosen. We opted for the basic straight-line target path to construct vector fields as shown in Figure 1(d). The current heading angle ψ is described as the angle between the direction of the robot's velocity and the positive y-axis, and the desired heading angle ψ^d is specified by the direction of the vector field. Let γ be the angle between the direction of the target straight path and the positive y-axis. $\tilde{d}$ represents the cross-track error denoting the distance of the robot from the target straight path. Particularly, we have $\dot{\tilde{d}} = V_g \sin(\psi - \gamma)$ with V_g being the ground speed [8]. ψ^∞ determines the magnitude of the desired heading angle when the cross-track error tends to be infinitely great. The desired heading angle is defined as

$$\psi^d(\tilde{d}) = -\psi^\infty \frac{2}{\pi} \arctan(k\tilde{d}) + \gamma, \tag{1}$$

where k is a positive constant that controls the rate at which the desired heading angle changes with cross-track error. We assume that the current heading angle change rate of the robot is defined by a first-order system

$$\dot{\psi} = a(\psi^c - \psi), \tag{2}$$

where ψ^c is the commanded heading, and a is a positive constant that characterizes the speed of response of the heading control. Let $\tilde{\psi} = \psi - \psi^d(\tilde{d})$ indicate the heading angle error. Considering a Lyapunov function candidate $W_1 = 1/2\tilde{\psi}^2$, then we get

$$\dot{W}_1 = \tilde{\psi}\left(a(\psi^c - \psi) + \psi^\infty \frac{2}{\pi} \frac{k}{1 + (k\tilde{d})^2} V_g \sin(\psi - \gamma)\right). \tag{3}$$

To make $\dot{W}_1 \leqslant 0$, we construct

$$\psi^c = \psi - \psi^\infty \frac{2}{a\pi} \frac{k}{1 + (k\tilde{d})^2} V_g \sin(\psi - \gamma) - \frac{\rho}{a} \mathrm{Sat}\left(\frac{\tilde{\psi}}{\varepsilon}\right), \tag{4}$$

* Corresponding author (email: weihe@ieee.org)

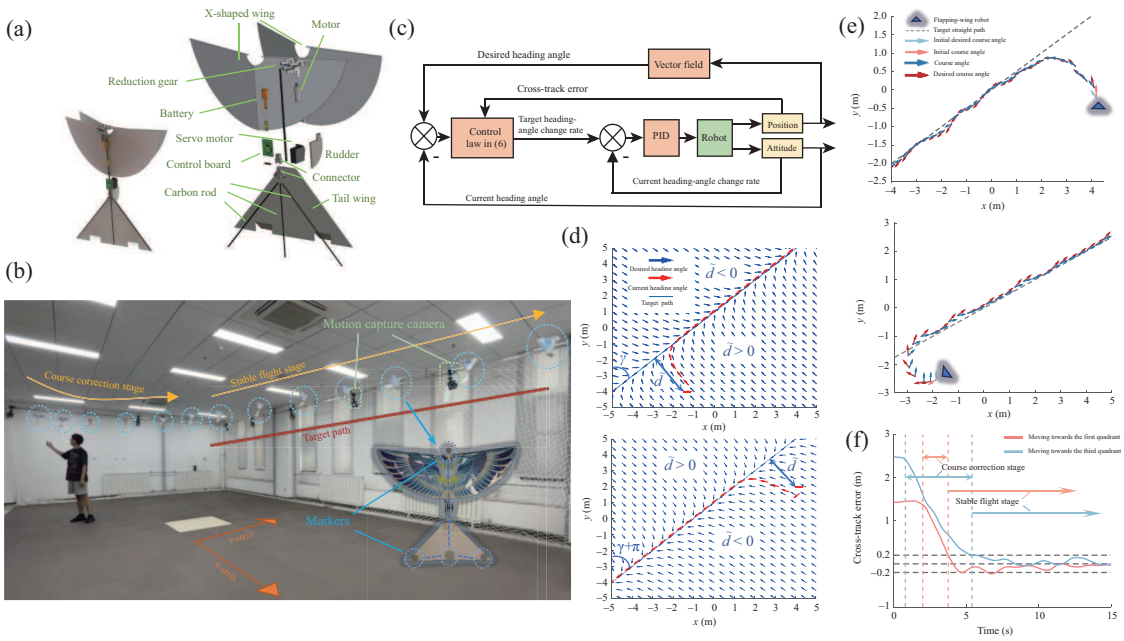

Figure 1 (Color online) Design, path following control and experiments of the micro flapping-wing robot. (a) The designed micro flapping-wing robot. Utilizing the X-shaped wing enhances fuselage stability, enabling the robot to hover in an almost upright position. Meanwhile, by maneuvering the tail rudder to obstruct the airflow generated by wing flapping, rapid, flexible, and controllable turning becomes achievable. These demonstrate the advanced advantages of our designed flapping-wing robot in terms of maneuverability and reliability. (b) Experimental setup. (c) The control block diagram of the path following algorithm. (d) Simulation results. (e) Experimental results. (f) Cross-track errors in the experiments.

where the Sat function is defined as

$$\mathrm{Sat}(x)=\begin{cases} x, & \text{if } |x|\leqslant 1,\\ \mathrm{sign}(x), & \text{otherwise,}\end{cases} \tag{5}$$

ρ is used to regulate the trajectory of the robot as it approaches the target route, while ε governs the width of the transition region. ε plays a role in mitigating chattering issues in proximity to the sliding surface. Substituting (4) into (2), the final target heading angle change rate applied to the robot is defined as

$$\dot{\psi}=-\psi^{\infty}\frac{2}{\pi}\frac{k}{1+(k\tilde{d})^2}V_g\sin(\psi-\gamma)-\rho\mathrm{Sat}\left(\frac{\tilde{\psi}}{\varepsilon}\right). \tag{6}$$

It remains to show that the system trajectories asymptotically converge to the origin $(\tilde{d},\tilde{\psi})=(0,0)$, another Lyapunov function candidate is introduced as $W_2=1/2\tilde{d}^2+1/2\tilde{\psi}^2$. Taking the derivative yields

$$\begin{aligned}\dot{W}_2=&\tilde{d}V_g\sin(\psi^d(\tilde{d})+\tilde{\psi}-\gamma)-\rho\tilde{\psi}\mathrm{Sat}\left(\frac{\tilde{\psi}}{\varepsilon}\right)\\ \leqslant&-\rho\tilde{\psi}\mathrm{Sat}\left(\frac{\tilde{\psi}}{\varepsilon}\right)+V_g\tilde{d}\sin(\psi^d(\tilde{d})-\gamma)\\ &+V_g|\tilde{d}|\,|\sin(\psi^d(\tilde{d})+\tilde{\psi}-\gamma)-\sin(\psi^d(\tilde{d})-\gamma)|\\ \leqslant&-\rho\tilde{\psi}\mathrm{Sat}\left(\frac{\tilde{\psi}}{\varepsilon}\right)-V_g\tilde{d}\sin\left(\psi^{\infty}\frac{2}{\pi}\arctan(k\tilde{d})\right)\\ &+2V_g|\tilde{d}|\,|\tilde{\psi}|.\end{aligned} \tag{7}$$

Construct an auxiliary function

$$g(\tilde{d})=\begin{cases}\dfrac{2\psi^{\infty}k}{\beta\pi}\tilde{d}^2, & \text{if } |\tilde{d}|\leqslant M,\\ \dfrac{2\psi^{\infty}kM}{\beta\pi}(2|\tilde{d}|-M), & \text{if } |\tilde{d}|>M,\end{cases} \tag{8}$$

where M is an arbitrary constant. Let $f(\tilde{d})=\tilde{d}\sin(\psi^{\infty}\frac{2}{\pi}\arctan(k\tilde{d}))$, then $f(\tilde{d})$ and $g(\tilde{d})$ are both even functions. When $0\leqslant\tilde{d}<M$, we have

$$\begin{aligned}f'(\tilde{d})=&\sin\left(\frac{2\psi^{\infty}}{\Pi}\arctan(k\tilde{d})\right)\\ &+\frac{2\psi^{\infty}k\tilde{d}}{\pi}\left(\frac{\cos(\frac{2\psi^{\infty}}{\pi}\arctan(k\tilde{d}))}{1+(k\tilde{d})^2}\right)\\ \geqslant&\frac{4\psi^{\infty}k\tilde{d}}{\Pi}\left(\frac{1}{2}\frac{\cos(\frac{2\psi^{\infty}}{\pi}\arctan(kM))}{1+(kM)^2}\right)\\ \geqslant&g'(\tilde{d})=\frac{4\psi^{\infty}k\tilde{d}}{\beta\pi}\end{aligned} \tag{9}$$

under the condition of

$$\beta\geqslant\frac{2(1+(kM)^2)}{\cos(\frac{2\psi^{\infty}}{\pi}\arctan(kM))}. \tag{10}$$

Since $f(0)=g(0)$ and $f'(\tilde{d})\geqslant g'(\tilde{d})$, we have $f(\tilde{d})\geqslant g(\tilde{d})$ when $0\leqslant\tilde{d}<M$. Also note that, when $\tilde{d}>M$, we have

$$g(\tilde{d})\leqslant\frac{4\psi^{\infty}kM^2}{\beta\pi}\leqslant M\sin\left(\frac{2\psi^{\infty}}{\pi}\arctan(kM)\right)\leqslant f(\tilde{d}), \tag{11}$$

which leads to

$$\beta\geqslant\frac{4\psi^{\infty}kM}{\pi\sin(\frac{2\psi^{\infty}}{\pi}\arctan(kM))}. \tag{12}$$

To sum up, if

$$\beta\geqslant\max\left\{\frac{4\psi^{\infty}kM}{\pi\sin(\frac{2\psi^{\infty}}{\pi}\arctan(kM))},\frac{2(1+(kM)^2)}{\cos(\frac{2\psi^{\infty}}{\pi}\arctan(kM))}\right\}, \tag{13}$$

refer to (10) that for $|\tilde{d}| \leqslant M$, we get

$$\begin{aligned}\dot{W}_2 \leqslant & -\rho\tilde{\psi}\mathrm{Sat}\left(\frac{\tilde{\psi}}{\varepsilon}\right)+2V_g|\tilde{d}||\tilde{\psi}|-\frac{2V_g\psi^{\infty}k}{\beta\pi}\tilde{d}^2\\ \leqslant & -V_g\left(|\tilde{\psi}|\ \ |\tilde{d}|\right)\begin{bmatrix}\frac{\rho}{\varepsilon V_g} & -1\\ -1 & \frac{2\psi^{\infty}k}{\beta\pi}\end{bmatrix}\begin{pmatrix}|\tilde{\psi}|\\ |\tilde{d}|\end{pmatrix}.\end{aligned} \tag{14}$$

It is negative definite under the condition of

$$\frac{\rho}{\varepsilon V_g}\left(\frac{2\psi^{\infty}k}{\beta\pi}\right)>1. \tag{15}$$

For $|\tilde{d}|>M$, because $|\tilde{\psi}|<\pi$, we have

$$\begin{aligned}\dot{W}_2 \leqslant & -\rho\tilde{\psi}\mathrm{Sat}\left(\frac{\tilde{\psi}}{\varepsilon}\right)+2V_g|\tilde{d}||\tilde{\psi}|-\frac{2V_g\psi^{\infty}kM}{\beta\pi}(2|\tilde{d}|-M)\\ \leqslant & 2V_g\pi|\tilde{d}|-\frac{2V_g\psi^{\infty}kM}{\beta\pi}|\tilde{d}|\\ = & 2V_g\left(\pi-\frac{\psi^{\infty}kM}{\beta\pi}\right)|\tilde{d}|,\end{aligned} \tag{16}$$

which is less than zero if

$$\frac{\psi^{\infty}kM}{\beta\pi^2}>1. \tag{17}$$

Based on all the above derivation, we conclude that the system controlled by (1) and (6) is globally exponentially stable as $0<\psi^{\infty}\leqslant(\pi/2)$ and

$$\frac{2\psi^{\infty}k}{\beta\pi}\min\left\{\frac{\rho}{\varepsilon V_g},\frac{M}{2\pi}\right\}>1, \tag{18}$$

where β satisfies (13). Hence, the theoretical validation of path following algorithms utilizing vector fields has been established. To further reinforce this assertion, we opted for $y=x+1$ as the target straight path for simulation purposes. As depicted in Figure 1(d), the simulation results showcase the robot's capability to move in two opposite directions while adhering to the target line. The ground speed of the robot is set to be constant at 0.5 m/s. Over the course of a 15-second simulation, the cross-track error $\tilde{d}$ stabilizes at approximately 0.045 m, while the heading angle error $\tilde{\psi}$ settles within 5 degrees. These outcomes validate the effectiveness of the path following algorithm.

Experimental setup and results. The feasibility of implementing the vector field-based path following algorithm in the flapping-wing robot was validated through practical flight experiments utilizing a motion capture system. Figure 1(c) outlines the comprehensive control procedure employed during the experiment. Real-time flight data from the robot is acquired through the motion capture system and subsequently processed in the upper computer. The control law calculates the target heading angle change rate based on the vector field path following algorithm. Additionally, a proportion integration differentiation (PID) controller is employed to swiftly stabilize the heading angle change rate, ensuring it reaches the target value promptly. The experimental outcomes, depicted in Figure 1(e) with the target path set as $y=0.5x$, exhibit a smooth flight trajectory of the flapping-wing robot. After the trajectory correction stage, the robot adeptly adheres to the target path, steadily advancing in the predetermined direction. Figure 1(f) showcases the variation curves of the cross-track error for both experiments, illustrating a consistent decrease in the cross-track error throughout. Eventually, the error stabilizes within 0.2 meters in both experimental runs. It is observed that the cross-track error exhibits slight oscillations within the range of $[-0.2, 0.2]$ m. This behavior is attributed to the temporal delay in data acquisition by the upper computer from the motion capture system, causing discrepancies in calculating the robot's current angular velocity. Additionally, when the servo actuates the tail rudder for rotation, it might induce slight body vibrations, thereby introducing inaccuracies in the feedback of position and attitude information from the motion capture system. These factors contribute to errors in the path following process.

Conclusion and future work. This study involved the design of a micro flapping-wing robot capable of stable hovering flight, along with the establishment of a flight experimental platform based on the motion capture system for this robot. Through indoor flight tests, the feasibility of employing the proposed vector field algorithm for path following of the flapping-wing robot along a predetermined straight line was confirmed. In the future, efforts will concentrate on bolstering the flight stability of the robot while devising advanced tracking algorithms capable of navigating complex paths. This pursuit aims to achieve more precise and practical control of flapping-wing robots.

Acknowledgements This work was supported by National Natural Science Foundation of China (Grant Nos. 62303045, 62225304, 61933001), China Postdoctoral Science Foundation Funded Project (Grant No. 2023M730220), Postdoctoral Fellowship Program of CPSF (Grant No. GZC20230235), and Dreams Foundation of Jianghuai Advance Technology Center (Grant No. 2023ZM01Z023).

Supporting information Videos and other supplemental documents. The supporting information is available online at info.scichina.com and link.springer.com. The supporting materials are published as submitted, without typesetting or editing. The responsibility for scientific accuracy and content remains entirely with the authors.

References

1 Huang H, He W, Zou Y, et al. USTButterfly: a servo-driven biomimetic robotic butterfly. IEEE Trans Ind Electron, 2024, 71: 1758–1767
2 Zhu J H, Yang Y J, Wang X Y, et al. Attitude control of a novel tilt-wing UAV in hovering flight. Sci China Inf Sci, 2023, 66: 154201
3 Liu Y, Chen Z, Gao J, et al. High performance assembly of complex structural parts in special environments — research on space manipulator assisted module docking method. Robot Intell Autom, 2023, 43: 122–131
4 Zufferey R, Tormo-Barbero J, Guzman M M, et al. Design of the high-payload flapping wing robot E-flap. IEEE Robot Autom Lett, 2021, 6: 3097–3104
5 Huang H, He W, Wang J, et al. An all servo-driven bird-like flapping-wing aerial robot capable of autonomous flight. IEEE ASME Trans Mechatron, 2022, 27: 5484–5494
6 Jung W, Lim S, Lee D, et al. Unmanned aircraft vector field path following with arrival angle control. J Intell Robot Syst, 2016, 84: 311–325
7 Sujit P B, Saripalli S, Sousa J B. Unmanned aerial vehicle path following: a survey and analysis of algorithms for fixed-wing unmanned aerial vehicles. IEEE Control Syst Mag, 2014, 34: 42–59
8 Wang Y, Wang X, Zhao S, et al. Vector field based sliding mode control of curved path following for miniature unmanned aerial vehicles in winds. J Syst Sci Complex, 2018, 31: 302–324